Catalysis Today 161 (2011) 70–77

Contents lists available at ScienceDirect

Catalysis Today

journal homepage: www.elsevier.com/locate/cattod

Effect of ball milling on the characteristics of nano structure $SrFeO_3$ powder for photocatalytic degradation of methylene blue under visible light irradiation and its reaction kinetics

Mohammad Ghaffari[a,b,*], Pei Yun Tan[a], Muhammed Enes Oruc[b], Ooi Kiang Tan[a], Man Siu Tse[a], Mark Shannon[b]

[a] School of Electrical and Electronic Engineering, Nanyang Technological University, 50 Nanyang Avenue, Singapore 639798, Singapore
[b] Mechanical Science and Engineering, University of Illinois at Urbana-Champaign, Urbana, IL 61801, USA

ARTICLE INFO

Article history:
Received 12 June 2010
Received in revised form 8 November 2010
Accepted 10 November 2010
Available online 10 December 2010

Keywords:
$SrFeO_{(3-\delta)}$
Photocatalyst
Visible light
Methylene blue
Kinetic

ABSTRACT

In this report, $SrFeO_3$ photocatalyst powder was synthesized by a high temperature solid state reaction method and the size of the particle was reduced with a high energy ball milling machine. The morphology, crystalline structure, particle size and size distribution of obtained samples were characterized by energy dispersive X-ray spectroscopy (EDX), X-ray diffraction (XRD), UV–vis spectrometer, scanning electron microscope (SEM), and transmission electron microscopy (TEM). Photocatalytic activity of the prepared samples was investigated by photodegradation of methylene blue (MB). The obtained results show that the $SrFeO_3$ sample works as photocatalyst and by reducing the particle size using high energy ball milling method for 5 h milling, particles with 19–25 nm crystallite size exhibit maximum activity due to larger surface area. The photocatalytic activities of the powders were investigated and kinetics of reaction was modeled by using high performance liquid chromatography (HPLC) and Mass spectroscopy. Photocatalytic activities of these powders increase with decreasing particle size.

1. Introduction

Since 1972, [titanium dioxide, also named titania (TiO_2)] has been extensively studied as a photocatalyst due to its strong photo oxidizing potential, high stability, non-toxicity, and low cost [1]. However, the absorption pattern of pure TiO_2 has to be extended to the visible light region for efficient use of solar energy or indoor light. To address this requirement many studies were initially focused on doping titania with transition metals [2–4]. It was found that a metal dopant can be beneficial or detrimental depending on the type and concentration of the metal. Generally an increasing amount of a cation M in TiO_2 produces a shift of the absorption towards the visible light region. However, sometimes the shift is attributed to the segregation of M_2O_n agglomerates with no improvement in visible-light photoactivity [4]. Moreover, the incorporation of certain transition metal ions into TiO_2 is deleterious for photo oxidation [2]. Recently, visible-light activated photocatalytic titania have been obtained by doping nitrogen [5–10], carbon [11,12], sulphur [13,14], phosphorus [15] or fluorine [16]. Among the non-metallic dopants, publications are more devoted more to $TiO_{2-x}N_x$ materials. These anionic dopant species are found to be better than transition-metal dopants, with respect to stability of the doped materials, photocatalytic efficiency and ease of doping process [17]. However, a serious problem is associated with anion-doped TiO_2. The quantum yield of doped TiO_2 with visible-light irradiation is far lower than that of TiO_2 with UV irradiation. Miyauchi et al. reported that the quantum yield of undoped TiO_2 thin film was 18.5 with UV irradiation. After annealing in NH_3 at 400 °C, the quantum yield of N-doped TiO_2 thin film was 15.4 with UV, and 0.41 with visible [17–19].

As early as 1980, the photocatalytic property of $SrTiO_3$ oxide was known [20–23]. Similar to TiO_2, doping of $SrTiO_3$ was investigated to move its absorption to visible light range [23–36]. Another ferroelectric material, $SrFeO_3$, was found to possess redox behavior [27] and gas sensing properties [28,29]. In terms of bandgap energy, with increasing iron concentration, it was suggested that the bandgap reduced from 3.17 eV for $SrTiO_3$ to 1.80 eV for $SrFeO_3$ [30–32]. This paper describes a simple procedure for the preparation and synthesis of strontium ferrite photocatalyst by a solid-state reaction process and the photocatalytic activity was monitored using the decolorization of methylene blue (MB) under visible light. The crystal chemistry was comprehen-

* Corresponding author at: School of Electrical and Electronic Engineering, Nanyang Technological University, 50 Nanyang Avenue, Singapore 639798, Singapore. Tel.: +65 935 395 47.
E-mail addresses: moha0094@e.ntu.edu.sg, mgh@illinois.edu (M. Ghaffari).

0920-5861/$ – see front matter © 2010 Elsevier B.V. All rights reserved.
doi:10.1016/j.cattod.2010.11.031

sively characterized with HRTEM and quantitative X-ray diffraction (XRD).

2. Experimental

2.1. Materials synthesis

Strontium carbonate ($SrCO_3$) and iron oxide (Fe_2O_3) were obtained from Aldrich (99.9% pure). All reagents were of analytical grade and were used without further purification. Sigma–Aldrich and used as received. Titanium dioxide Degussa P25 nanoparticles (having 80% anatase and 20% rutile) in this study was provided by Degussa (Frankfurt, Germany) with a specific BET area of 50 $m^2\ g^{-1}$. Deionized water (18.2 MΩ cm) was used in all the experiment.

The synthesis of $SrFeO_3$ nanoparticles was carried out using a high temperature technique, where $SrCO_3$ and Fe_2O_3 powders were mixed in an agate mortar for 15 min. The mixture was calcinated at 1200 °C for 24 h and then the calcinated powder was then furnace cooled to room temperature and ground again in agate mortar for 15 min. Finally, the ground powder was further calcined again at 1200 °C for 24 h and furnace cooled to room temperature. The particle size of $SrFeO_3$ powder decreases by using ball milling process.

The milling of the $SrFeO_3$ solid solution powders were carried out using the high energy ball milling process. The tungsten carbide vials (volume of 250 mL) and balls (inner diameters of 10 mm and 20 mm) with relatively high density of 14.75 g/cm^3 were used for to increase the impact energy. The milling speed was set at 200 rpm and the balls-to-powder weight ratio was kept as 20:1. The milling was carried out using the planetary ball mill (Fritsch Pulverisette 5) in 30-min cycles with 25 min of milling followed by 5 min of pause to prevent overheating of the milling machine from the prolonged milling process.

2.2. Materials characterization

HRTEM and bright field images were collected using a Jeol JEM-2100F TEM instrument operated at 200 kV with 25 and 30 cm camera length. The selected area electron diffraction (SAED) patterns were also recorded with HRTEM to study the crystalline structure of the strontium ferrite. The pre-calcined specimens were prepared by dipping a carbon-coated copper grid into the dilute suspension. After calcination, the materials were ground gently and dispersed ultrasonically in water, and several drops of the suspension were deposited onto the grid. The electron diffraction pattern of anatase was simulated using JEMS Electron Microscopy Software.

The phase structure of the powders was identified using a Shimadzu Laboratory XRD-6000 instrument. Powder XRD patterns were collected over the 2θ angular range of 10–80° using Bragg-Brentano geometry (Cu Kα source, primary and secondary Soller slits, 0.1 mm divergence slits, 0.3 mm receiving slit, and secondary graphite monochromator). The diffractometer was calibrated against a laboratory standard (NIST SRM 660a).

The surface morphology and the status of the sample were observed with scanning electron microscopy (SEM) (JEOL 6335F). The compositional and elemental analysis was carried out with energy dispersive spectroscopy (EDS) (Oxford). At given intervals of visible illumination, a specimen of the methylene blue remaining was collected and analyzed by UV–vis spectroscopy (Shimadzu 2450).

2.3. Photocatalytic activity

In order to test the photocatalytic behavior of the $SrFeO_{(3-\delta)}$ (SFO) samples, photodegradation of methylene blue in water has been chosen as a test reaction. The photocatalytic reaction was conducted in a 50 mL cell culture vessel with continuous magnetic stirring. The as-prepared SFO was used as photocatalyst and mixing of DI water with methylene blue (MB, 0.0313 M for10.8 μmol/L) used as control sample, moreover all the data compare with results of Degussa P25 particle in the same condition. Four tubes (12-in.), 8-W fluorescent tubes (UVP Inc.) were used as the illumination light sources. P25 TiO_2 powders as standard photocatalyst were also used in the photoactivate experiments as a comparison. Aqueous solutions of methylene blue (MB, 0.0313 M for10.8 μmol/L) and photocatalyst particles (pure TiO2, SFO particles and Degussa P25 were placed in a cell culture vessel. Finally at given intervals of fluorescent illumination the Uv–visible spectra of all samples from 400 nm to 800 nm were collected and remaining concentration of MB, obtained and analyzed by Shimadzu 2450 spectrophotometer. To investigate the kinetics of methylene blue, JIS R 1703-2 2007 standard was used and absorbance value of MB was taken by fixing the wavelength at 664 nm. The remaining methylene blue in suspension was collected and also in all experiment used one control samples with out any catalyst to compare the results with it.

2.4. Product analysis and identification using LC–UV/vis–MS studies

The chromatographic experiments with Agilent 1100 LC/MSD Trap XCT Plus system were carried out on a HP 1100 liquid chromatograph (Agilent, USA) using a binary solvent gradient pump and an automatic injector. The mobile phase consisted of two solutions namely A and B. Solution A was made from 0.1% formic acid and acetic water, whereas solution B was acetonitrile. The flow rate was 400 μl/min .The dye degradation products were separated using Agilent Zorbax SB-C18 column 2.1 × 50 mm, 3.5 μm. The detection system was a diode array detector (Agilent, USA) with detection range between 200 and 780 nm. The gradient HPLC separation was coupled with, ion trap mass spectrometer (Agilent Technologies). The mass spectrometer was equipped with an electrospray ionization source and operated in positive polarity. The mass range was from 50 to 700 m/z. The ESI conditions were as follows: capillary voltage: 3.5 kV, endplate offset was fixed at 500 V; skimmer at 40 V; trap drive at 53 V; the nebulizer pressure was 35 psi; drying gasflow was 8 L min^{-1} and the drying temperature was 350 °C.

3. Results and discussion

3.1. Characterization of nanopowder

To identify the crystalline structure of the strontium ferrite nanopowders, XRD analysis was performed on the samples. The results from the XRD are presented in Fig. 1. This figure shows

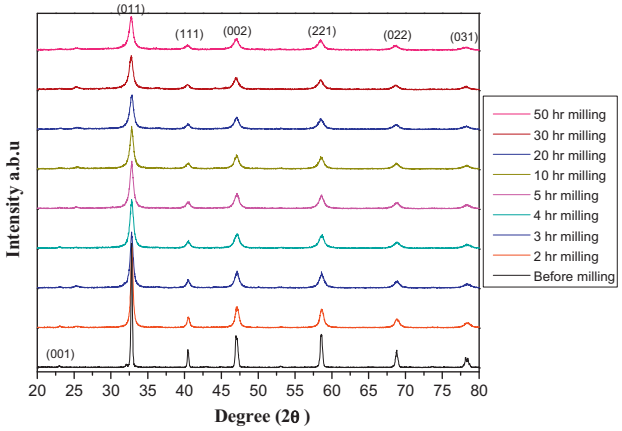

Fig. 1. Powder XRD patterns of high temperature $SrFeO_3$ for different milling time.

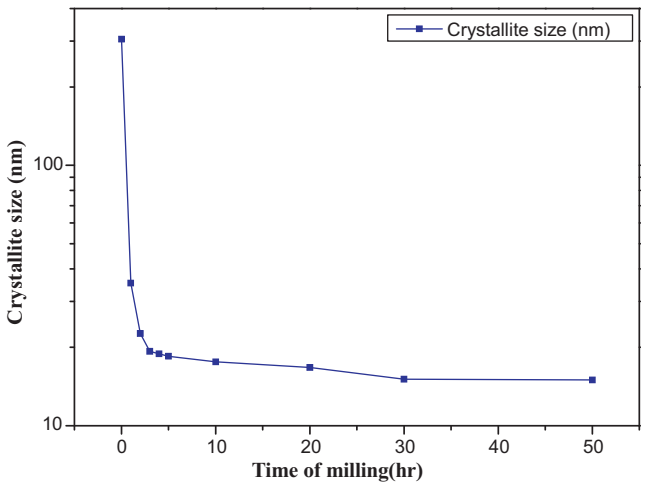

Fig. 2. Crystallite size of high temperature $SrFeO_3$ with increasing milling time.

decreasing crystallite size with increasing time of milling from the peak broadening. The crystallite size of strontium ferrite calculated using Rietveld quantitative analysis.

Fig. 2 shows the average crystallite sizes of the ball-milled $SrFeO_3$ powders as a function of ball milling time .The crystallite size was calculated using Rietveld analysis and the results showed that mechanical alloying is highly effective in reducing crystallite size with increasing milling time. This figure depicts three separate processing steps. During the first step, a rapid decrease in average crystallite size of $SrFeO_3$ occurs from 0 to 3 h of milling. With increasing milling time, the large powder particles were broken into smaller particles due to cold welding and plastic deformation that consequently led to the crystallite size decrease. In the second step from 3 h to 30 h of milling only a further small decrease in crystallite size occurred, the crystallite size of powder decreased because with increasing milling time the dislocation density increased and severe plastic deformation (SPD) occurred. During the last step, the crystallite size remained about the same. This is because of saturation of the hardening process and the crystallite size did not change a lot [37–39].

Figs. 3 and 4 show the TEM images of $SrFeO_3$ nanoparticles. Selected area electron diffraction (SAED) patterns confirm the strontium ferrite crystallite (Fig. 3b). Figs. 3b and 4b present the indexing of $SrFeO_3$ powder with [1 1 1] zone axis before and after 5 h milling. These diffractions show after 5 h of milling the single crystallite structure of the particles was converted to fine grained (nanocrystalline) form material based on the ring SAED pattern. This image confirms the XRD result that shows reduction in crystallite size after 5 h milling, because during high-energy milling the powder particles were repeatedly flattened, cold welded, fractured and rewelded. By achieving smaller particle size, and increasing defects such as deformation and dislocations, the particles can decrease their free energy to reach a stable stage [40].

The SEM micrographs of the strontium ferrite particles before milling (Fig. 5(a)), after 5 h (Fig. 5(b)) and 50 h milling (Fig. 5(c)) presents high level of agglomeration after 50 h milling due to the high tendency to decrease the surface energy after 5 h milling. The EDS pattern of pure strontium ferrite particles after 5 h milling is presented in Fig. 6, which shows that the $SrFeO_3$ nanoparticles consist of Sr, Fe, Cu and O elements (Fig. 6) without any contamination from other elements. The copper element comes from the copper grid used for SEM sample preparation.

Fig. 7 shows the size distribution of $SrFeO_3$ nanoparticles. Fig. 7 refers to size distribution of the pure $SrFeO_3$ before and after 2, 5, and 30 h milling. The average particle size of the particles gradually decreases with milling times. However variation of particle size is not very significant after 5 h milling.

3.2. Photocatalytic activity

The experiment of photocatalytic reaction was conducted in a 50 mL cell culture vessel with continuous magnetic stirring. The as-prepared SFO was used as photocatalyst, and mixing of DI water with methylene blue (MB, 0.0313 M for10.8 μmol/L) was used as a control sample. Moreover all the data are compared with results using Degussa P25 particle in the same condition. Fig. 8 presents the absorbance of MB under visible light illiminution from 0 to 12 h. Strontium ferrite powders with different particle size and time of milling were chosen to investigate the photocatalytic activity of the nanopowders and sampling was done for 0, 1, 2, 3, 5, 7, 10 and 12 h.

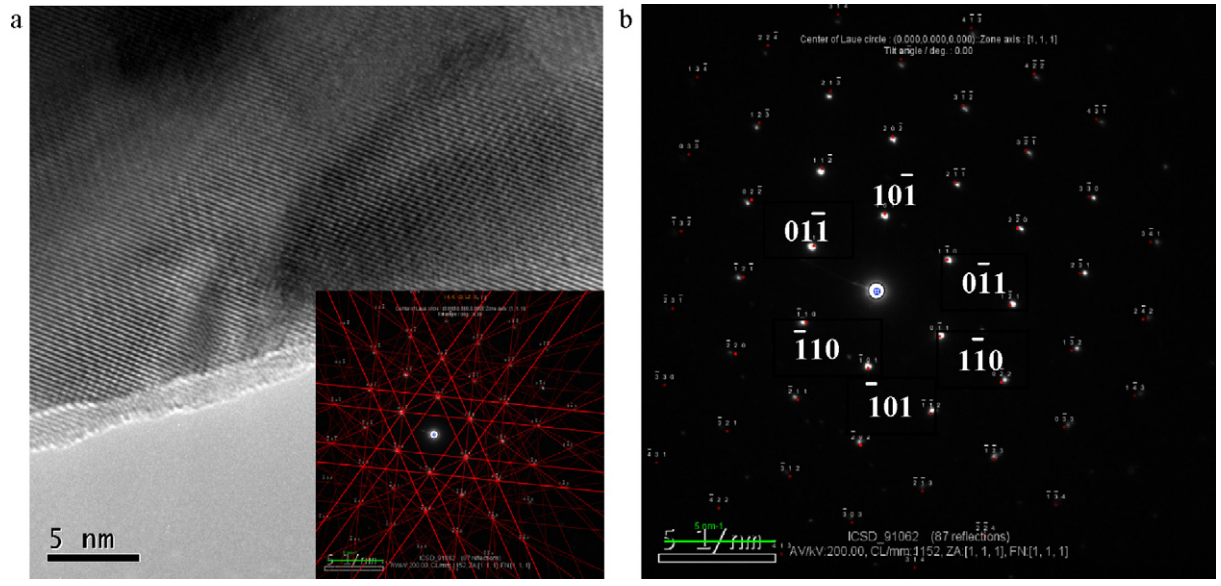

Fig. 3. (a) TEM micrographs of $SrFeO_3$ single-crystal nanoparticles before milling with related Kikuchi patterns and (b) single-crystal electron diffraction pattern that could be indexed as strontium ferrite with [1 1 1] zone axis.

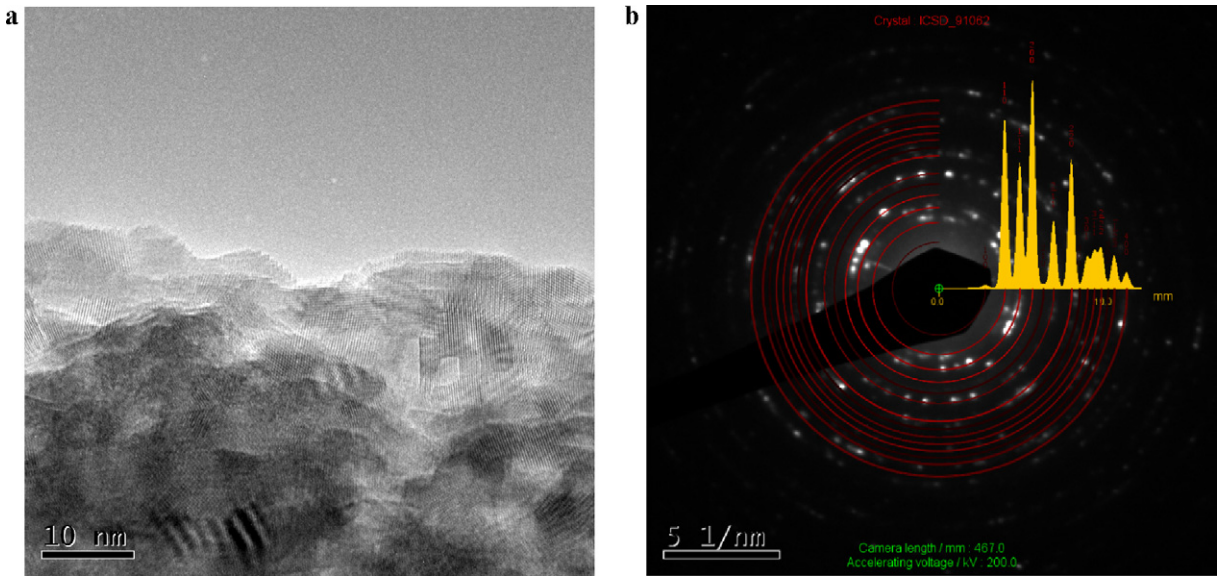

Fig. 4. (a) TEM micrographs of $SrFeO_3$ fine grained (nanocrystalline) material. After 5 h milling (b) ring diffraction pattern obtained from a fine grained (nanocrystalline) material. The SAED patterns could be indexed as strontium ferrite with [1 1 1] zone axis.

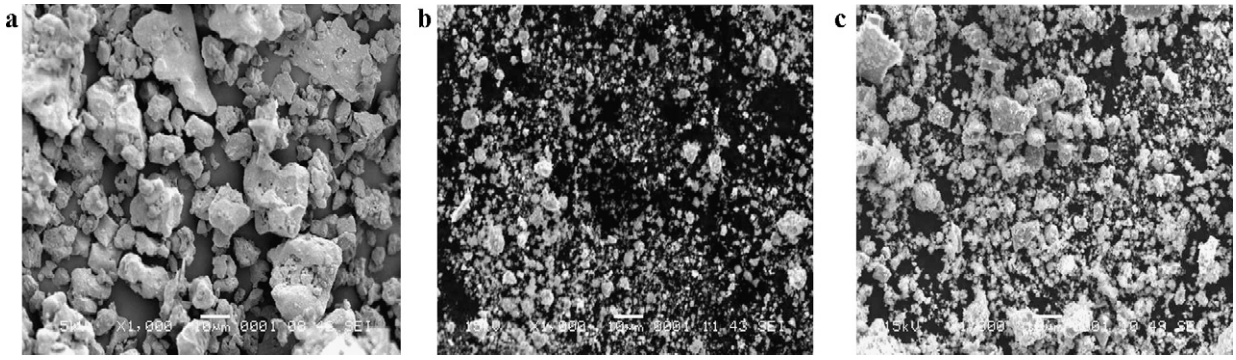

Fig. 5. (a) SEM micrograph of the strontium ferrite particles before milling, ×1000; (b) SEM micrograph of the strontium ferrite particles after 5 h milling, ×1000 and (c) SEM micrograph of the strontium ferrite particles after 50 h milling ×1000.

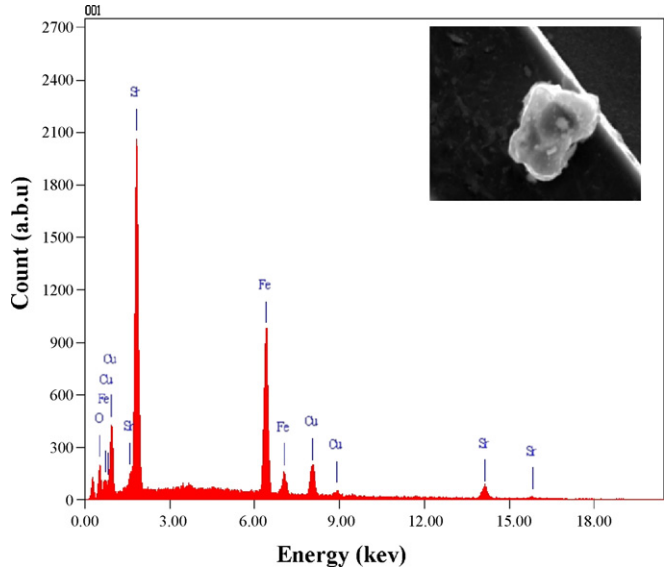

Fig. 6. EDX spectra of the $SrFeO_3$ nanoparticles after 5 h milling and related structure.

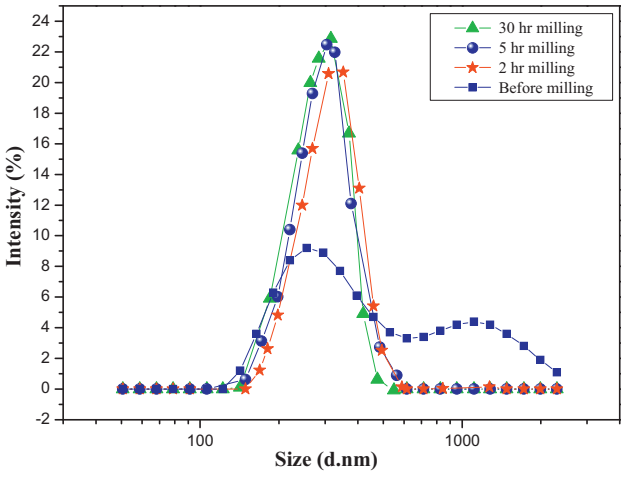

Fig. 7. The size and size distribution of $SrFeO_3$ nanoparticles before and after milling.

Fig. 9 shows a plot of C/C_0 versus time for all the experiments of photocatalytic decomposition, where C_0 is the initial concentration of methylene blue. The results demonstrate that degradation was faster in the solution with finer powder, which can be ascribed to

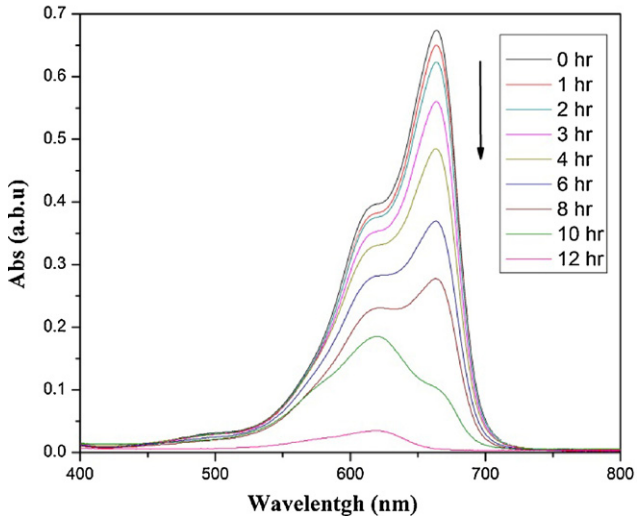

Fig. 8. Absorbance of methylene blue under visible illumination from 0 to 12 h.

the increase in surface area and the number of active sites on the finer powder.

Fig. 9 also shows that the performance of high temperature $SrFeO_3$ sample after 5 h milling is not much different compared with the sample milled up to 30 h and 50 h. This can be explained by Fig. 7, which shows that the crystallite size of high temperature $SrFeO_3$ powder reaches a minimum at 4–5 h ball milling. Therefore, the optimal ball milling time for high temperature $SrFeO_3$ powder is 5 h. Beyond 5 h, the photocatalytic performance of high temperature sintering $SrFeO_3$ powder does not improve any further.

3.3. Kinetic modeling

Based on literature reports, the chemical kinetic of photocatalytic dye oxidation in liquid systems can be described by a first-order model with respect to dye concentration. Using this hypothesis, the reaction rate for second order surface decomposition of methylene blue can be written in terms of Langmuir–Hinshelwood kinetics [41,42]. The Langmuir–Hinshelwood model can be written as

$$r = k\frac{K[C]}{1+K[C_0]} = k_{obs}[C], \tag{1}$$

$$\frac{1}{k_{obs}} = \frac{1}{kK} + \frac{C_0}{k}, \tag{2}$$

where C_0 is the initial concentration of methylene blue (MB) (ppm), K is the Langmuir–Hinshelwood adsorption equilibrium constant (ppm^{-1}), k is the second order rate constant of surface reaction ($ppm\,min^{-1}$), and k_{obs} is the pseudo-first-order rate constant (min^{-1}) that satisfies

$$-\frac{dC}{dt} = k_{obs}C_0, \tag{3}$$

giving

$$-\ln\left(\frac{C}{C_0}\right) = k_{obs}t, \tag{4}$$

For the case of methylene blue (MB) the Langmuir–Hinshelwood kinetics can be given by

$$r = -\frac{d[MB]}{dt} = -\frac{kK[MB]}{1+K[MB]_0}, \tag{5}$$

where r is the rate of dye mineralization, k is the rate constant, [MB] is the dye concentration, and K is the adsorption coefficient. The implicit solution for (5) is

$$\ln\left(\frac{[MB]}{[MB]_0}\right) + K([MB]-[MB]_0) = -kKt. \tag{6}$$

Eq. (6) can be solved explicitly for t by using discrete changes in $[MB]$ from the initial concentration to a zero reference point.

The model presented in Eq. (6) yields an exact solution for the degradation of methylene blue. However, when the concentration is in the scale of millimoles, an apparent first-order model can be assumed [43], such that

$$r = -\frac{d[MB]}{dt} = k'[MB] = kK[MB]. \tag{7}$$

Integration results in either

$$[MB] = [MB]_0 e^{-k't}, \tag{8}$$

$$\ln\left(\frac{[MB]_0}{[MB]}\right) = -kKt = -k't, \tag{9}$$

where k' is in units of $time^{-1}$. The assumption of a pseudo-first order model was used in several studies to characterize the effect of different experimental conditions on the degradation rate [44,45].

Fig. 10 shows the results of methylene blue degradation by SFO powder under visible light illumination. The semi log data plot does not produce a single straight line, hence does not fit a simple first-order reaction model for the entire period of visible illumination examined. This plot presents three linear regions that can be explained by series of reaction mechanism. Fig. 10 suggests a series of reaction mechanism for photocatalytic degradation of organic dyes, described by

$$\text{Organic Dye } (MB) \xrightarrow{k_1} \text{absorbed by surface of powder} \xrightarrow{k_2} \text{intermediate products} \xrightarrow{k_3} \text{colorless products} \xrightarrow{k_4} \text{surface saturation} \tag{10}$$

In the first stage of reaction, the methylene blue absorbed by surface of powder. It means first some amount of methylene blue absorbed by surface of powder and then the reaction between our material and methylene blue start that is good point. Then the

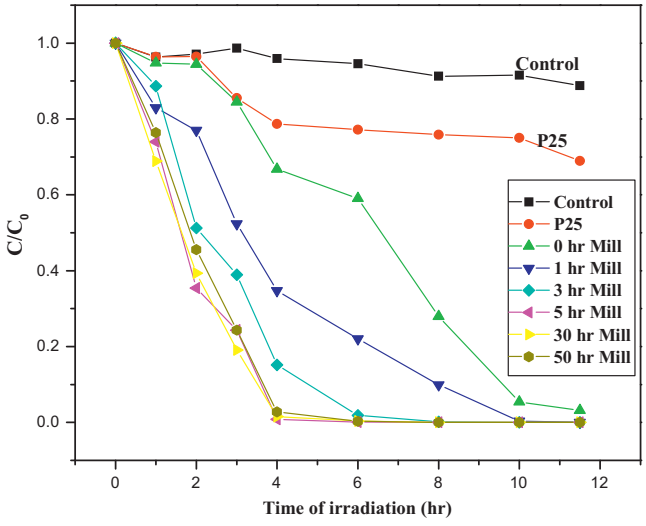

Fig. 9. Methylene blue degradation by high temperature SFO powder with different milling time.

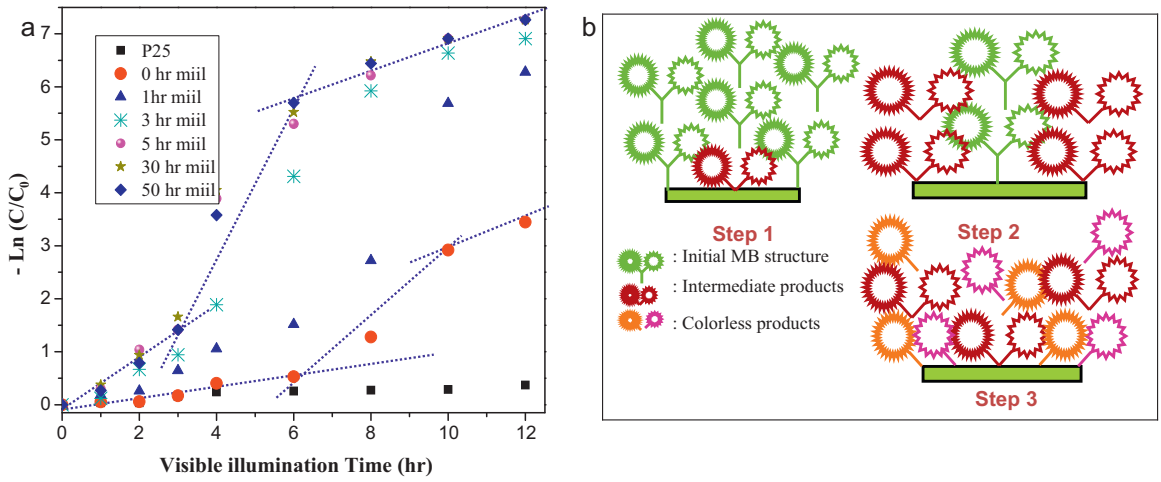

Fig. 10. (a) Data plot of methylene blue degradation by SFO powder under visible light illumination and (b) schematic of series of reaction.

organic dyes were degraded to intermediate products. The reaction rate for this step *CD* is described by Eq. (11). After this step, the intermediate products, *CI* were transformed to colorless products, with reaction rate given by Eq. (12). Finally, the surface of the powder particles was saturated by intermediate and colorless products and the reaction rate decreased [46].

If the consumption reactions of the dye and intermediate are both first-order, and *CI* can be described with respect to time by

$$\frac{d[C_D]}{dt} = -k_2 C_D \Rightarrow C_D = C_D \exp(-k_2 t), \quad (11)$$

$$\frac{d[CI]}{dt} = k_2 C_D - k_3 C_I \Rightarrow C_I = \left(\frac{k_2 C_D}{k_3 - k_2}\right)(\exp(-k_2 t) - \exp(-k_3 t)). \quad (12)$$

Table 1 presents the reaction rate at each step that calculated from the slopes of a straight line obtained by plotting $-\ln(C/C_0)$ versus reaction time (Fig. 10). The results show that the $Step_1$, $Step_2$ and $Step_3$ for P25 is constant, which can be explained by the fact that P25 works under UV-light and is not sensitive to visible light. For milled powder (more than 3 h) the slope of $Step_3$ is smaller than $Step_2$ due to saturation of the powder surface. The reaction rate of this step is lower than step two but for the case of 0 and 1 h milled powder because the surface of powder is lower, the reaction rate of first step ($Step_1$) is not as high as with 3 h milled powder, so the saturation case in step three is negligible. This table also confirms that the optimized time for milling is 5 h to achieve optimum reaction rate.

3.4. Product analysis and identification using HPLC–MS studies

To obtain a better insight into the catalytic mechanism of the $SrFeO_3$ powders with methylene blue (MB), the degradation of methylene blue, under both dark and light conditions was measured. 10 mg of $SrFeO_3$ powders were dispersed in DI water and added to the MB solution with 10 ppm concentration. The initial pH value of the $SrFeO_3$ and MB solution at both dark and light conditions were 9.35 and 9.15 respectively. For this experiment a precise continuous setup was used to investigate the methylene blue degradation and by products in situ. Fig. 11 presents the methylene blue degradation for the dark and light conditions.

Table 1
Kinetic rate constants of methylene blue (MB) at various ball-mill time.

Samples	$k_{Step\,1}$ (h^{-1})	$k_{Step\,2}$ (h^{-1})	$k_{Step\,3}$ (h^{-1})
P25	0.03	0.0281	0.0271
0 h milled	0.061	0.2548	0.4958
1 h milled	0.191	0.5019	0.7699
3 h milled	0.3147	1.0195	0.246
5 h milled	0.4727	0.8791	0.2623
30 h milled	0.515	0.9057	0.2062
50 h milled	0.4344	0.9025	0.2056

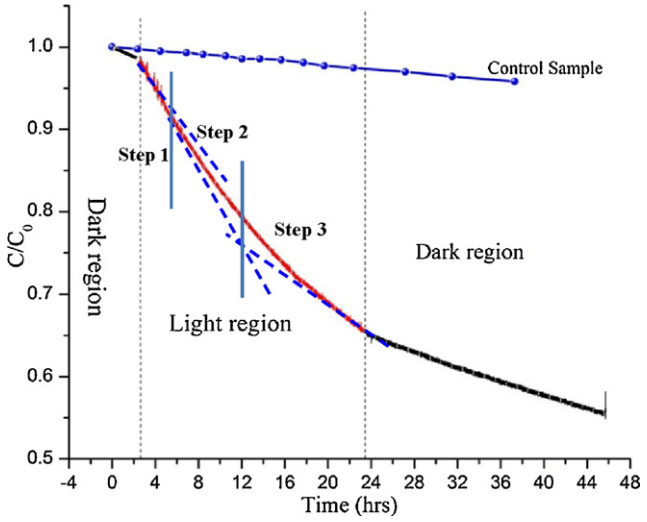

Fig. 11. Methylene blue degradation by high temperature SFO powder in light and dark region.

As shown in Fig. 11, a degradation of methylene blue in dark condition was observed. This can be explained as the self-degradation of methylene blue at basic pH values. The slope of the curve in light condition increased, compared with the two dark condition. This higher rate can be explained by the increase in the degradation of methylene blue in the presence of light. In addition the slope for the light condition is not exactly a linear and can be explained by three different steps including (initiation, propagation and termination) in the following section (Fig. 10).

The chromatographic separation of the dye solution initially and during the photocatalytic process were recorded and monitored. To show that the degradation of methylene blue occurs in three steps, several sampling in dark and light condition were made and the by-product of the reactions analyzed using the HPLC equipment. The gradient HPLC separation was coupled with the ion trap mass spectrometer. The degradation of the dye may possibly be cap-

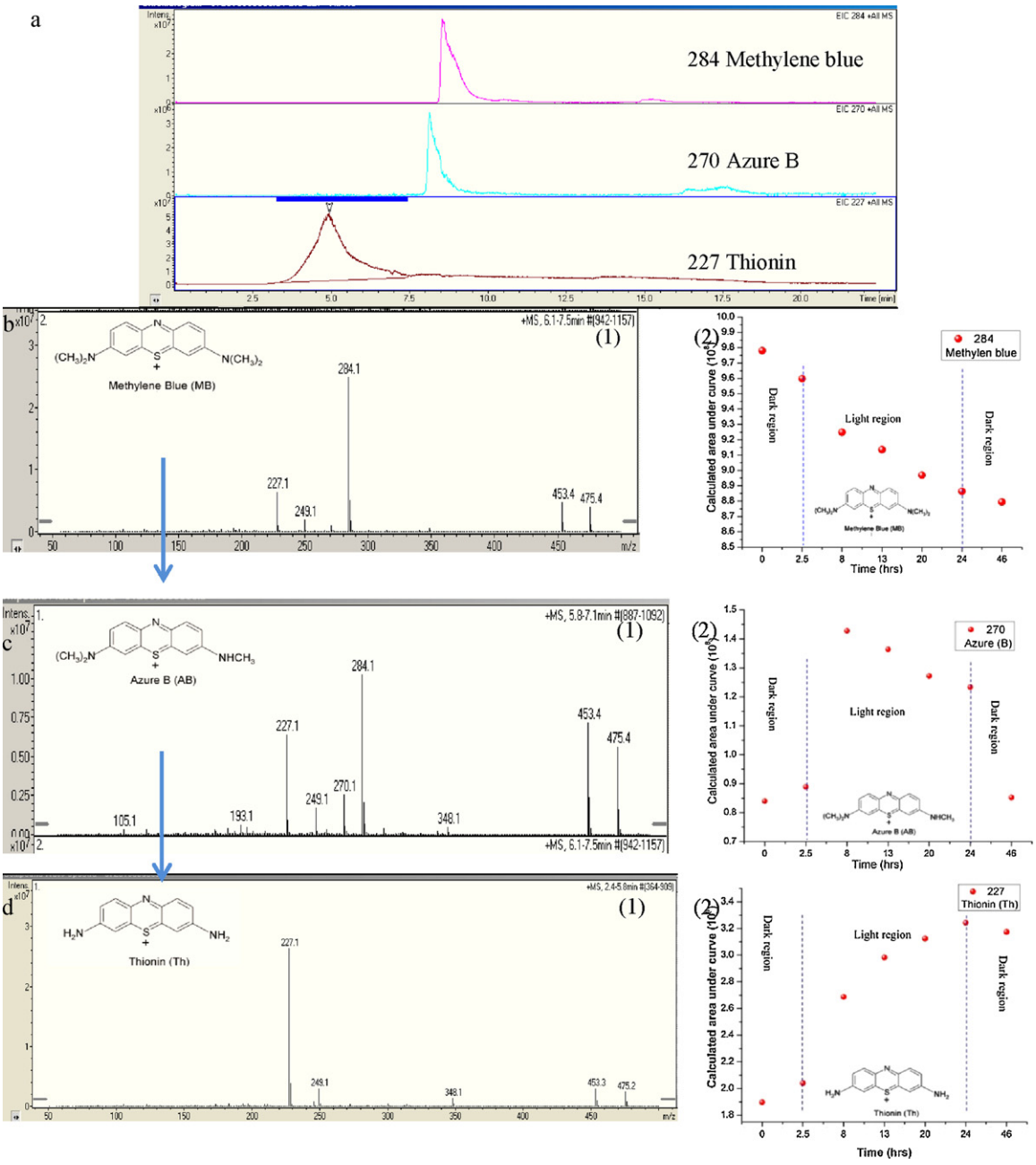

Fig. 12. (a) HPLC peaks for methylene blue (284) azure B (270) and thionin (227) and mass spectra of the major detected degradation intermediates (b) for methylene blue peak (c) azure B (d) thionin and (2) it is related area under curves.

tured by the qualitative analysis of the samples studied by HPLC before and after photocatalytic degradation. Further analysis of the product formation was done by mass spectroscopic (MS) studies of the degradation intermediate products and the results are shown in Fig. 12. Many peaks of different intensities were observed in addition to the peak of methylene blue dye, which indicated the variation in the composition and concentration of the degradation products. By studying some of these intermediate masses and predicting their structure by the cleavage of one or more of the methyl groups substituent on the amine groups, that led to the production of intermediate products, it was found that there was agreement in their masses with the intermediates formed. For instance, the formation of azure B and thionin (Fig. 12) through the demethylation cleavage during the photocatalytic degradation has been reported in the literature [47,48]. From the HPLC peak area calculations, it was found that methylene blue structure break into the azure B and then cleavage to thionin. As expected methylene blue structure degraded even in the dark condition (Fig. 12b.2). However the slope of part under light in comparison with the two parts under dark is higher and can be explained by the increase in the degradation of methylene blue in the presence of light. Moreover the rate of producing the Azure B increased when the light was turned on (Fig. 12.c.2) and after further exposure to light decreased because at the same time this intermediate product started to breakdown and produced the thionin.

4. Conclusion

In this work, we have successfully prepared photocatalytic strontium ferrite particles using a high temperature solid state reaction method. Determining the optimal processing condition requires adjustment of ball milling time. The single phase nano

materials show better photocatalytic degradation of methylene blue in the visible light compared to P25. The improved performance of samples milled for 5 h relative to samples milled for more or less time is attributed the optimum particle size, providing large reaction area.

References

[1] A. Fujishima, Nature 238 (1972) 37.
[2] E. Reddy, B. Sun, P. Smirniotis, The Journal of Physical Chemistry B 108 (2004) 17198.
[3] H. Haick, Y. Paz, The Journal of Physical Chemistry B 107 (2003) 2319.
[4] F. Gracia, J.P. Holgado, A. Caballero, A.R. Gonzalez-Elipe, The Journal of Physical Chemistry B 108 (2004) 17466.
[5] C. Rhee, S. Bae, J. Lee, Chemistry Letters 34 (2005) 660.
[6] Y. Nosaka, M. Matsushita, J. Nishino, A.Y. Nosaka, Science and Technology of Advanced Materials 6 (2005) 143.
[7] H. Matsui, H. Tabata, N. Hasuike, H. Harima, B. Mizobuchi, Journal of Applied Physics 97 (2005) 123511.
[8] D. Li, H. Haneda, S. Hishita, N. Ohashi, Chemistry of Materials 17 (2005) 2588.
[9] S. Yang, L. Gao, Journal of the American Ceramic Society 87 (2004) 1803.
[10] M. Mrowetz, W. Balcerski, A. Colussi, M. Hoffmann, The Journal of Physical Chemistry B 108 (2004) 17269.
[11] H. Wang, J. Lewis, Journal of Physics: Condensed Matter 17 (2005) L209.
[12] Y. Li, D. Hwang, N. Lee, S. Kim, Chemical Physics Letters 404 (2005) 25.
[13] J.C. Yu, W. Ho, J. Yu, H. Yip, P.K. Wong, J. Zhao, Environmental Science and Technology 39 (2005) 1175.
[14] T. Ohno, M. Akiyoshi, T. Umebayashi, K. Asai, T. Mitsui, M. Matsumura, Applied Catalysis A: General 265 (2004) 115.
[15] L. Lin, W. Lin, Y. Zhu, B. Zhao, Y. Xie, Chemistry Letters 34 (2005) 284.
[16] J. Yu, J. Yu, W. Ho, Z. Jiang, L. Zhang, Chem. Mater 14 (2002) 3808.
[17] C. Burda, Y. Lou, X. Chen, A. Samia, J. Stout, J. Gole, Nano letters 3 (2003) 1049.
[18] M. Miyauchi, A. Ikezawa, H. Tobimatsu, H. Irie, K. Hashimoto, Physical Chemistry Chemical Physics 6 (2004) 865.
[19] G. Torres, T. Lindgren, J. Lu, C. Granqvist, S. Lindquist, The Journal of Physical Chemistry B 108 (2004) 5995.
[20] C. Wagner, D. Zatko, R. Raymond, Analytical Chemistry 52 (1980) 1445.
[21] S. Ahuja, T. Kutty, Journal of Photochemistry and Photobiology A: Chemistry 97 (1996) 99.
[22] T. Ishii, H. Kato, A. Kudo, Journal of Photochemistry and Photobiology A: Chemistry 163 (2004) 181.
[23] R. Konta, T. Ishii, H. Kato, A. Kudo, The Journal of Physical Chemistry B 108 (2004) 8992.
[24] M. Miyauchi, M. Takashio, H. Tobimatsu, Langmuir 20 (2003) 232.
[25] T. Ohno, T. Tsubota, Y. Nakamura, K. Sayama, Applied Catalysis A: General 288 (2005) 74.
[26] E. Bakken, S. Stølen, T. Norby, R. Glenne, M. Budd, Solid State Ionics 167 (2004) 367.
[27] Y. Wang, J. Chen, X. Wu, Materials letters 49 (2001) 361.
[28] C. Liang, D. Yang, Z. Yang, F. Hou, M. Xu, Surface and Coatings Technology 200 (2005) 2515.
[29] R. Moos und, K.H. Härdtl, Journal of the American Ceramic. Society 80 (1997) 2549.
[30] V.L. Kozhevnikov, I.A. Leonidov, M.V. Patrakeev, E.B. Mitberg, K.R. Poeppelmeier, Journal of Solid State Chemistry 158 (2001) 320.
[31] A. Rothschild, W. Menesklou, H.L. Tuller, E. Ivers-Tiffée, Chemistry of Materials 18 (2006) 3651.
[32] D. Smith, E. Chang, D. Liu, Phase Transitions 58 (1996) 57.
[33] J. Davidson, D. Myers, M. Chakraborty, No Time to Waste: Poverty and the Global Environment. 1992.
[34] N. Cheremisinoff, P. Cheremisinoff, R. Tratter, Chemical and Nonchemical Disinfection, Ann Arbor (1981).
[35] USAID. Washington, D.C.: United States Agency for International Development, 1990, p. l.
[36] W. Xiao, New materials systems for advanced tribological and environmental applications. 2006.
[37] M.T. Marques, V. Livramento, J.B. Correia, A. Almeida, R. Vilar, Journal of Alloys and Compounds 434–435 (2007) 481.
[38] C. Galán, A. Ortiz, F. Guiberteau, L. Shaw, Journal of the American Ceramic Society 92 (2009) 3114.
[39] H. Zuhailawati, Y. Mahani, Journal of Alloys and Compounds 476 (2009) 142.
[40] C. Suryanarayana, Progress in Materials Science 46 (2001) 1.
[41] A. Linsebigler, G. Lu, J. Yates Jr., Chemical Reviews 95 (1995) 735.
[42] S. Irmak, E. Kusvuran, O. Erbatur, Applied Catalysis B: Environmental 54 (2004) 85.
[43] I. Konstantinou, T. Albanis, Applied Catalysis B: Environmental 49 (2004) 1.
[44] S. Lakshmi, R. Renganathan, S. Fujita, Journal of Photochemistry and Photobiology A: Chemistry 88 (1995) 163.
[45] T. Zhang, T. Oyama, A. Aoshima, H. Hidaka, J. Zhao, N. Serpone, Journal of Photochemistry and Photobiology A: Chemistry 140 (2001) 163.
[46] A. Julson, D. Ollis, Applied Catalysis B: Environmental 65 (2006) 315.
[47] C. Yogi, K. Kojima, N. Wada, H. Tokumoto, T. Takai, T. Mizoguchi, H. Tamiaki, Thin Solid Films 516 (2008) 5881.
[48] A. Orendorz, C. Ziegler, H. Gnaser, Applied Surface Science 255 (2008) 1011.